Effects of image focal depth in geometrical lightguide head mounted displays

Xu, Miaomiao, Hua, Hong

Miaomiao Xu, Hong Hua, "Effects of image focal depth in geometrical lightguide head mounted displays," Proc. SPIE 11310, Optical Architectures for Displays and Sensing in Augmented, Virtual, and Mixed Reality (AR, VR, MR), 113100N (19 February 2020); doi: 10.1117/12.2543264

SPIE.

Event: SPIE AR VR MR, 2020, San Francisco, California, United States

Effects of image focal depth in geometrical lightguide head mounted displays

Miaomiao Xu* and Hong Hua
3D Visualization and Imaging Systems Laboratory, College of Optical Sciences, University of Arizona, 1630 East University Boulevard, Tucson, AZ 85721, USA

ABSTRACT

Waveguide or lightguide has the advantages of light weight, small volume and relatively high efficiency and thus is considered as one of the promising solutions to the optical combiner required for optical see-through augmented reality displays. Although there exist a few commercial products utilizing lightguides as the optical combiners, few works discussed the potential image artifacts caused by the ray bundle collimation errors in lightguides. In this paper, we discussed three causes of collimation errors in the geometrical waveguide: lightguide manufacture tolerance, change of image focal depth, and curved lightguide substrate. Based on the simulation and experiment results of the first two causes, we demonstrated two different types of image artifacts in the geometrical-waveguide-based AR displays.

Keywords: head mounted display, waveguide combiner, 3D display

1. INTRODUCTION

Nowadays waveguide is regarded as one of the most promising combiner optics in the optical see-through head-mounted display (OST-HMD) system. A typical waveguide combiner is a several-millimeter-thick plate which combines the virtual image with the real world scene by total internal reflection (TIR). The waveguide optics can be classified into different types by their out-couplers, the functional part of the waveguide that breaks TIRs of the input rays and couples the rays into the eyes. Different technologies are explored and utilized in the out-couplers, including surface relief gratings (SRGs) [1-3], volume hologram (VHs) [4-8], resonant waveguide gratings (RWGs) [9], metasurfaces [10], partially reflective mirror arrays (PRMA) [11-13] and microstructure mirror arrays (MMAs) [14-18]. Among all these different types, the last two can be categorized as geometrical waveguide (or lightguide), since the out-coupling mechanisms are based on reflections. Compared with other types of waveguides that are based on diffractive optical elements, the geometrical lightguides are less sensitive to the incident angle and wavelength of the coupling rays and have the advantages of easy manufacture and molding, thus are promising solutions to the combiner optics in OST-HMDs.

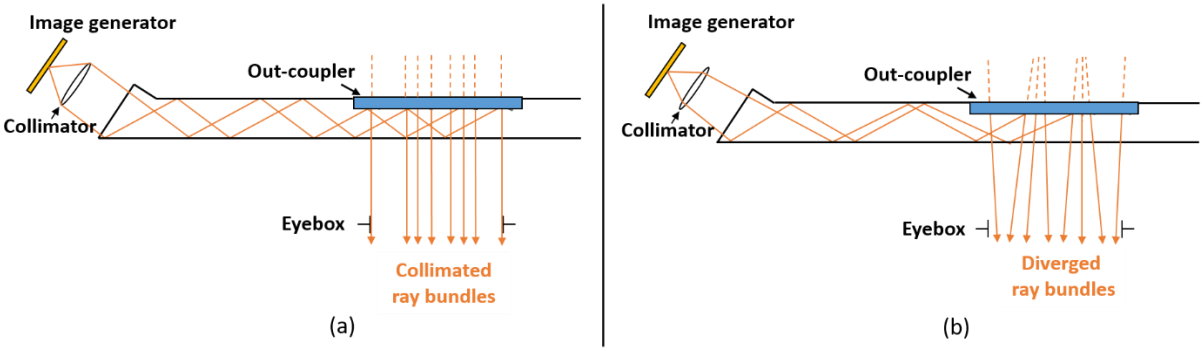

Fig. 1. (a) Schematic layout of a typical lightguide-based OST-HMD with the virtual image at optical infinity. (b) Schematic layout of a lightguide-based OST-HMD with the virtual image at a finite depth. Some image artifacts may arise due to the pupil replication at the out-coupler area or discontinued out-coupler structure.

Figure 1(a) shows a schematic layout of a typical lightguide-based OST-HMD when the virtual image is at the optical infinity. The system mainly consists of an image generator, a collimator and a lightguide. The image generator renders the virtual image, the collimator magnifies the virtual image from the image generator to the optical infinity, and the

Optical Architectures for Displays and Sensing in Augmented, Virtual, and Mixed Reality (AR, VR, MR), edited by Bernard C. Kress, Christophe Peroz, Proc. of SPIE Vol. 11310, 113100N

lightguide guides the light from the image generator to the eyebox. When the image is at the infinity, the image perceived by the eye is free from the artifact caused by pupil replication at the lightguide out-coupler area. That is because when a ray bundle is collimated, the viewer will see all the rays reflected from the out-coupler coming from infinity in the same direction. This case, however, is no longer valid when the image focus change, as shown in Fig. 1(b). When the displayed image is at a finite depth, the ray bundles from the microdisplay become diverged. Due to the discontinued out-coupler structures or the duplicated pupils at the out-coupler area, a ray bundle from the finite virtual image will split into several ray paths, which causes the perceived image to have ghost-like image artifacts.

Several cases may cause the image focus change and lead to the image artifacts in the lightguide-based systems, which also give the significance of studying the image performance and artifacts in this paper. First, some manufacture or alignment errors of the collimator may cause some inevitable collimation errors of the ray bundles before they are coupled into the lightguides, which leads to image degradation. Secondly, the non-parallelism between the two waveguide substrate surfaces or the non-parallelism between each segment of the out-coupler can induce collimation errors of the ray bundles. Thirdly, due to the increased demanding of designing a curved or Bizarre-shaped optical combiner with optical power, studying the image performance and artifacts when the image is at different depth becomes necessary. In this paper, we aim to analyze the image performance and artifacts of the geometrical lightguide system when the collimation errors of the ray bundle occur and the nominal focus depth of the virtual image is not at the optical infinity. To demonstrate the image artifacts, we show the simulation and experimental results based on the MMA geometrical lightguide, whose simulation and design methods have been discussed in detail in our previous work [17, 18]. The rest of this paper is organized as follows. The image artifacts caused by the non-parallelism in the lightguide are discussed in Section 2. By using Monte Carlo simulation, the relationships between the physical parallelism and image artifacts are quantified. The image artifacts caused by ray collimation or image focus depth change are discussed in Section 3. Two different types of artifacts are demonstrated in this section. To validate our discussion, we setup a prototype and present experiments in Section 4 to demonstrate the image artifacts when the focus depth changes.

2. IMAGE ARTIFACTS CAUSED BY UN-PARALLELISM TOLERANCES IN LIGHTGUIDE

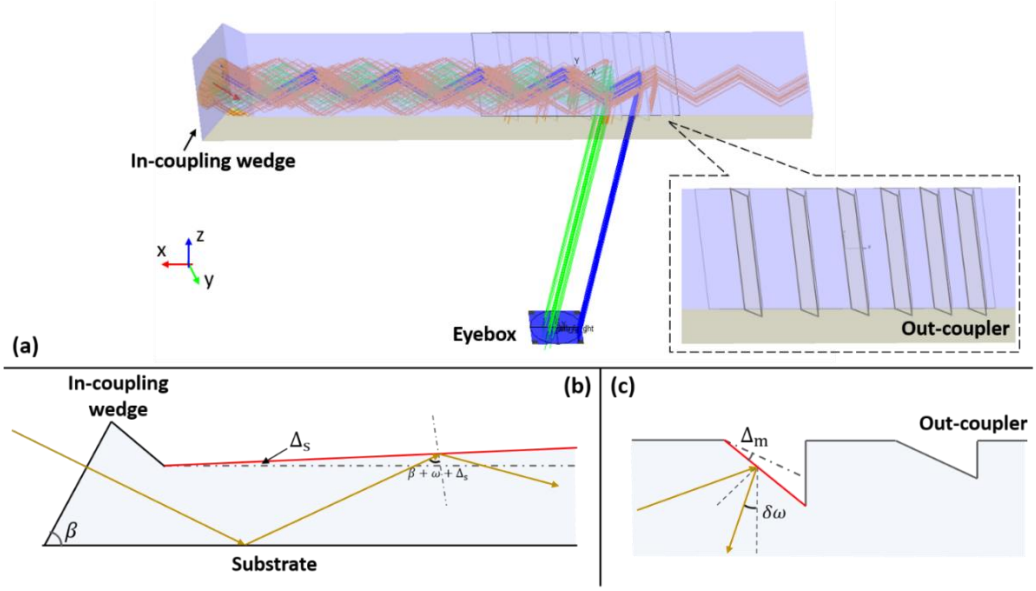

Fig. 2. (a) Schematic layout of the MMA-based lightguide. (b) and (c): Causes of the ghost-like image artifacts in MMA-lightguide by lightguide manufacture tolerance. (b) The un-parallelism between the two substrate surfaces and (c) the un-parallelism between adjacent slanted mirrors.

The MMA-based geometrical waveguide mainly contains three parts: the in-coupling wedge, the waveguide substrate and the out-coupler area, as shown in Fig. 2(a). The position of the in-coupling wedge surface matches with the exit pupil location of the collimator, so that the ray bundle from the collimator can be coupled into the waveguide substrate without light loss. The out-coupler area is formed by an array of cascaded slanted mirrors, whose angle is designed to couple out the image to the viewer's central line of sight. Two cases related to the lightguide manufacture tolerances may cause the ghost-like image artifacts in the MMA-lightguide, as shown in Fig. 2(b) and 2(c) respectively. In the first

case, the ray collimation error is induced due to a small wedge between the two surfaces of the lightguide substrate, as shown in Fig. 2(b). When a ray bundle from field angle ω is coupled into the lightguide, a small wedge angle Δ_s leads to the angle of propagation error to be $\delta\omega = 2\Delta_s$ after each pair of TIRs in the lightguide substrate. Finally, the segmented ray paths have a collimation error $n \cdot \delta\omega$, which results from nth TIRs pairs when propagating in the substrate. In the second case, the ray collimation error is induced by the small wedge error Δ_m of the segmented slanted mirrors at the out-coupler area, as shown in Fig. 2(c). It leads to the out-coupled ray deviate $\delta\omega = 2\Delta_m$ from its designed field angle ω, which also induces collimation error between the segmented ray paths reflected from adjacent segmented mirrors. To differentiate the two types of errors, we named them as multiple reflections induced (MR) and micro-mirror array induced (MMA) collimation errors hereafter.

To evaluate how the lightguide manufacture tolerances affect the perceived image and how much ghost-like image artifact can be seen over the entire image, we simulated the ray propagation in a raytracing software like LightTools®. The geometrical model of the lightguide is shown in Fig. 2(a), whose configuration is well designed and has been discussed in [18]. The lightguide out-coupler contains six segmented mirrors, and is optimized by uniformity bias merit function (See [18]). The system has a field of view (FOV) of 26° (H) x 15.6° (V), and the ray bundles from 1280 different horizontal field angles are sampled during the simulation. The most straightforward way to simulate the image error is to vary the wedge Δ_s and Δ_m in the configuration, trace ray bundles over the entire field and simulate the perceived image and its ghost images. However, it requires long computation time, especially when running Monte Carlo simulation with thousands of configurations assigning different amount of wedge angles. An alternative way to do the simulation is to analyze the ray paths of each ray bundle from different field angles, categorize the ray bundles by their ray paths and calculate the image artifacts by the potential manufacture tolerance experienced by the ray paths. In this method, raytracing only needs to be done once, which saves a lot of computational time. After obtaining the ray path information (including which segmented mirrors couple out the ray bundles and the number of TIRs that the ray bundles experienced before coupled out), the image errors can be calculated by the post-assigned manufacture tolerances in each element and the relationship between the ray deviation angle and the manufacture tolerances.

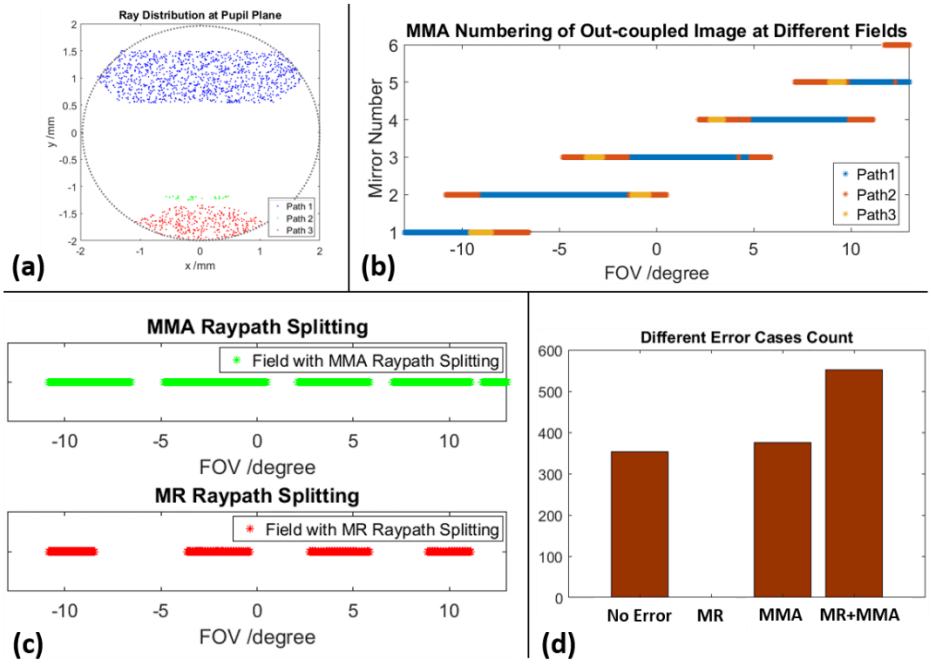

Fig. 3. Raytracing results of the lightguide which correlates the ray collimation error with the manufacture tolerances. (a) A ray bundle footprint distribution at the pupil plane, 3 ray paths are labeled with 3 colors. (b) The segmented mirror numbers at which the ray paths are coupled out over the FOV. (c) The distributions of MMA-induced and MR-induced ray path splitting over the entire FOV and (d) the statistical result of 4 different ray collimation error types (1280 sampled field angles in horizontal).

Figure 3 shows the ray path sorting results based on our simulation model. The first step is to trace each ray bundle from different field angles and get the number of ray paths, which are differentiated by the different number of TIRs or the

different segmented micro-mirrors. Figure 3(a) shows an example of an out-coupled ray footprint distribution at the eyebox, where three different ray paths are labeled with different colors. To get the relationship between the ray paths and the segmented micro-mirrors, the micro-mirrors are labeled as the number 1-6 from the ray coming direction to the far end, and the correspondence between the ray paths and the out-coupled micro-mirror number is plotted in Fig. 3(b). The ray bundles from different field angles are then sorted by different types of ray path splitting induced by different tolerances. Figure 3(c) shows the distributions of the two collimation error types over the entire field of view, and Figure 3(d) shows the statistical result of the overall 1280 sampled ray bundles with different cases of collimation errors encountered during propagation.

After we characterized the ray bundles by their ray paths and their encountered tolerance types, the next step is to assign the amount of tolerances of each element and calculate the corresponding collimation errors. Randomized manufacture tolerances with Gaussian probability density functions are assigned to the substrate wedge Δ_s and the mirror wedges Δ_{m1}~Δ_{m6} for 6 segmented micro-mirrors respectively, whose 3σ full width are [-6, +6] arcsecs (for Δ_s) and [-9, +9] arcsecs (for $\Delta_{mi}, i = 1\sim6$), respectively. Figure 4(a) shows the angular subtense distribution of the ghost-like image artifacts over the entire FOV when the wedge errors Δ_s and Δ_{mi} are -0.024, -2.49, -1.38, -0.75, 0.86, 2.56 and -2.19 arcsecs. After running Monte Carlo simulation for 3000 trials, the distributions of the field average and the worst ghost-like image angular subtense are plotted in Fig. 4(b) and 4(c) respectively. 80% configurations have the average subtense less than 5.91 arcsecs and the worst subtense less than 16.65 arcsecs over the FOV. It is worth noting that the wedge tolerance in our simulation is very tight with high precision manufacture, but it can be scaled linearly to a loose tolerance to match with the commercial manufacture capabilities.

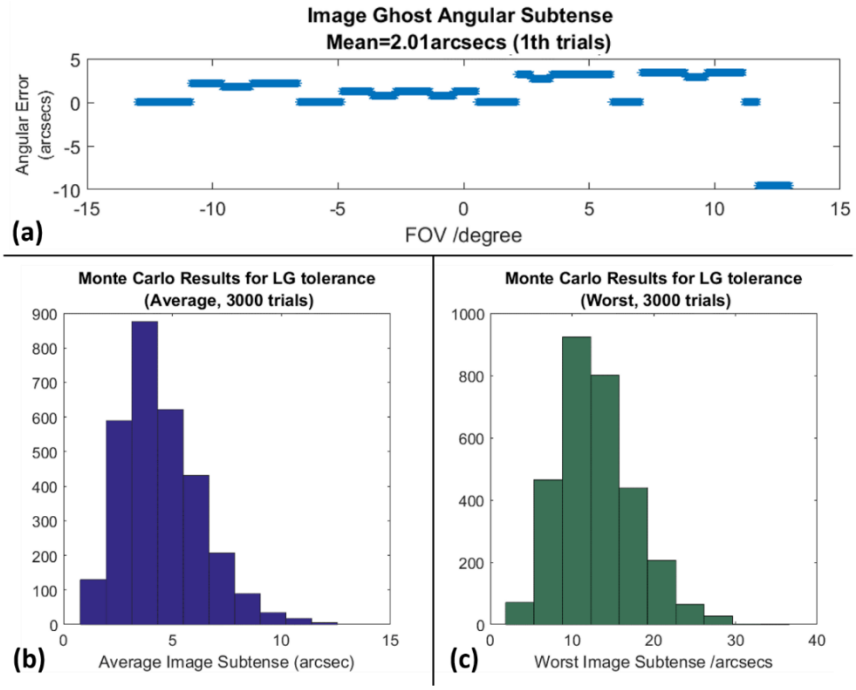

Fig.4. Results of the ghost-like image artifact subtense (angular error between the images from different ray paths seen by eyes). (a) The image ghost angular subtense over the entire FOV when the Δ_s and Δ_{mi} are randomly assigned as -0.024, -2.49, -1.38, -0.75, 0.86, 2.56 and -2.19 arcsecs. (b) The distributions of the field average image ghost subtense in 3000 trials and (c) the distributions of the worst image ghost subtense in 3000 trials.

3. IMAGE ARTIFACTS CAUSED BY THE CHANGE OF IMAGE FOCUS DEPTH

The ghost-like image artifacts caused by the image focus depth change are discussed in this section. Most of the existing waveguides or lightguides in OST-HMDs require the virtual image to be at the optical infinity, so that the ray bundles from the microdisplay are collimated when coupled into the lightguide. Since the ray bundles will keep the collimation during propagation, the eye will receive a ghost-free image as if all the rays coupled in from the same direction also couples out in the same direction in visual space. However, it is infeasible in practice, since there is inevitable

collimation error caused by axial position mismatch between the microdisplay and collimator, which results in imperfect collimated ray bundles. Figure 5(a) shows an example when the microdisplay is axially moved closer to the collimator, which intentionally introduces large collimation errors of the in-coupled ray bundles. It is clearly seen that the displayed 1-pixel-width white lines split into several lines, due to the image focus depth change and the induced ray collimation error.

Figure 5(b) and 5(c) demonstrated the two ray paths that cause the ray collimation errors in the MMA-based lightguide. In the first case, the ray bundle is split into different ray paths by the segmented micro-mirrors in the out-coupler area. The displacement between each micro-mirror baseline causes a slight image displacement of each ray path. The resulted image artifacts are similar as in Fig. 5(b), where the images are displaced with small angular amounts. This type of artifact occurs over the entire FOV if the image focus depth is not at the optical infinity, and its angular subtense is not significantly affected by the change of the image focus depth. Another case is shown in Fig. 5(c), where the ray bundle splitting occurs at the lightguide substrate, since some of the ray paths experience twice more TIRs than the other ray paths before coupled out. This kind of artifact acts differently as the first type, as the image angular separation is much larger than the previous type due to much larger OPDs between different ray paths, and the angular subtense of the image artifacts highly related to the image focus depth change. Nonetheless, this kind of ray bundle splitting only occurs within a narrow field range, which does not affect the overall image performance as significantly as the previous case. Since the ray path splittings are also induced by either different numbers of TIRs (pupil replication) or the discontinued micro-mirrors, we also named the two ghost-like artifacts as MR-induced and MMA-induced artifacts.

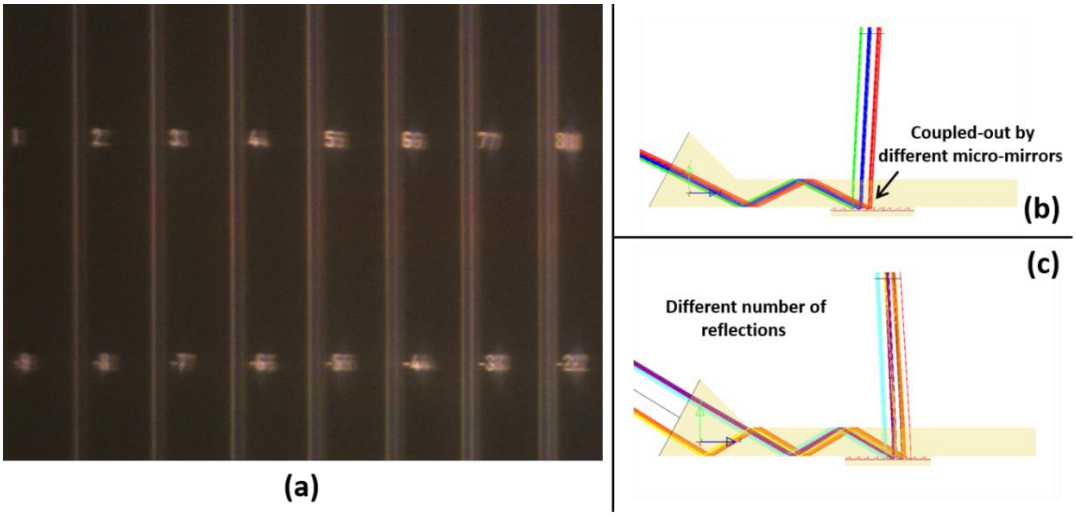

Fig. 5. (a) Image artifacts captured from an MMA-based lightguide. Two different ray path splittings can induce the ghost-like artifacts in the MMA-lightguide: (b) artifacts caused by different micro-mirror reflections (MR-induced artifacts) and (c) artifacts caused by different numbers of reflections in substrate before the rays reach the out-coupler area (MMA-induced artifacts).

4. EXPERIMENTAL RESULT

Based on the discussions in Section 2 and Section 3, we can conclude that the ghost-like artifacts caused either by manufacture tolerance or by the image depth change in the lightguide-based systems can be identified into two types: One is called MR-induced artifact, which is induced during the propagation in lightguide due to the multiple TIRs; another is called MMA-induced artifact, which is induced at the out-coupler region due to the segmented micro-mirrors displacement. To validate the demonstrations in Section 2 and Section 3, we implemented a proof-of-concept monocular prototype of an MMA-lightguide-based OST-HMD as shown in Fig. 6. An LCoS microdisplay with a built-in illumination engine with a resolution of 1280 by 960 served as the image generator. It is mounted on a one-axis translation stage, so that the image focus depth in visual space can be varied by axially moving the LCoS. A commercial collimator was utilized, which was mounted with the lightguide to ensure pupil match. The lightguide has a dimension of 51mm (L) x 4.39mm (W) x 16mm (H), with a 61.67° in-coupler wedge angle and an out-coupler area of 13.3mm (L) x 1.53mm (W) x 16mm (H). A machine vision camera was placed at the eye box of the MMA-lightguide with 4mm entrance pupil size to capture the out-coupled image performance.

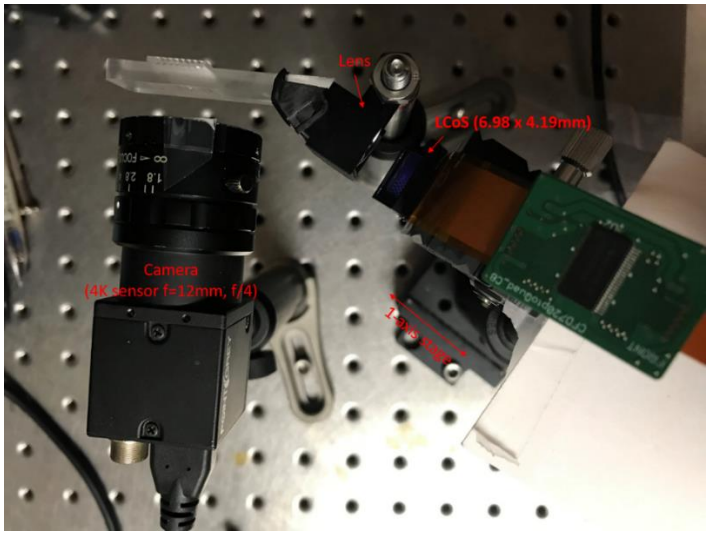

Fig. 6. Experimental setup of the MMA-based lightguide system.

To observe the image artifacts at different focal depths, we axially changed the position of LCoS to vary the displayed virtual image depth in visual space. Two image depths are selected as a comparison: 0.25D and 2.6D. Figure 7 shows the camera captured image for the two cases. Two resolution targets at 0.25D and 2.6D are placed at the see-through pass to show the camera focus. It is clearly seen the MR-induced image artifact in -5° to -2° field range when the virtual image is at 2.6D, as the checkerboards split into two in this area and the slant purple edge shifted horizontally, as shown in Fig. 7(b). Contrastingly, the MR-induced image artifact is not apparent when image focal depth is at 0.25D (Fig. 7(a)), because the angular subtense of the MR-induced artifact highly depends on the change of focal depth. The MMA-induced artifact, although degrades the image contrast, is not shown obviously in Fig.7, since we displayed an image with low spatial resolution contents. The MMA-induced artifact is shown more obviously when displaying high spatial frequency image information like the 1-pixel-width white line as discussed previously. The captured image is shown in Fig. 7(b) when the focal depth of the virtual image is at 2.6D, showing ghost-like image artifacts across the entire field of view.

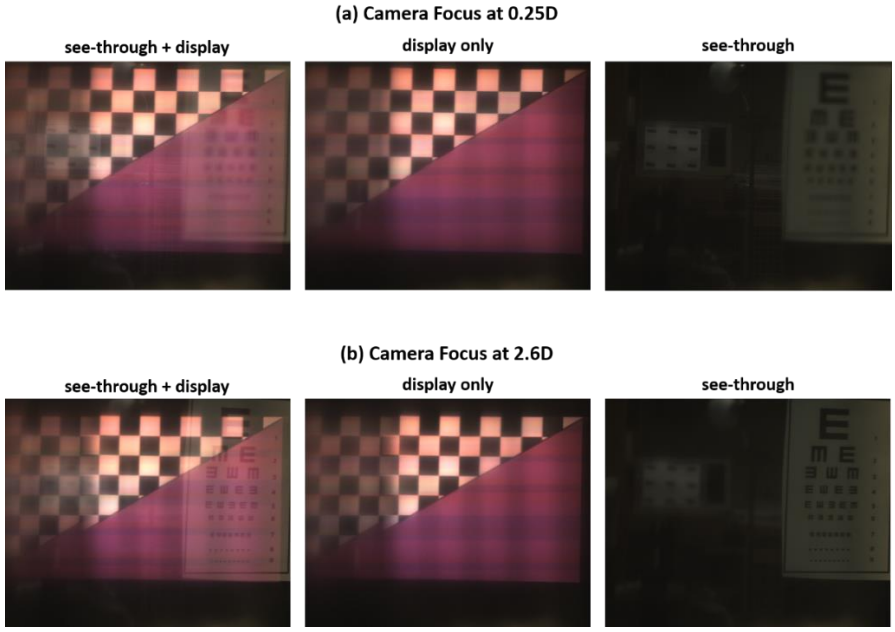

Fig. 7. Camera captured image when image focal depths are (a) 0.25D and (b) 2.6D. Each row shows the captured images when enable see-through and virtual display, enable only virtual display, and enable only see-through path.

5. CONCLUSION

In this paper, we demonstrated the image artifacts caused by ray collimation errors in the geometrical lightguide. Three typical conditions may lead to ray collimation errors and cause image artifacts: lightguide manufacture tolerance, change of image focal depth, and curved lightguide substrate. We analyzed the ray propagation paths of the first two cases, and concluded that there are two major causes which induced the ray paths splitting and image artifacts: artifacts induced by multiple reflections and artifacts induced by different out-coupler segments. Future works can be done by analyzing the image performance quantitatively by MTF test or plot, simulating the influence of the artifacts to the retinal image, and characterizing the relationship between the image focal depth and the amount of error.

REFERENCE

[1] B. C. Kress and W. J. Cummings, "11‐1: Invited Paper: Towards the Ultimate Mixed Reality Experience: HoloLens Display Architecture Choices," SID Symposium Digest of Technical Papers 48(1), 127-131 (2017).

[2] T. Levola and P. Laakkonen, "Replicated slanted gratings with a high refractive index material for in and outcoupling of light," Opt. Express 15(5), 2067-2074 (2007).

[3] P. Äyräs, P. Saarikko, and T. Levola, "Exit pupil expander with a large field of view based on diffractive optics," Journal of the Society for Information Display 17(8), 659-664 (2009).

[4] Z. Lv, J. Liu, J. Xiao, and Y. Kuang, "Integrated holographic waveguide display system with a common optical path for visible and infrared light," Opt. Express 26(25), 32802-32811 (2018).

[5] J. D. Waldern, A. J. Grant, and M. M. Popovich, "17‐4: DigiLens AR HUD Waveguide Technology," SID Symposium Digest of Technical Papers 49(1), 204-207 (2018).

[6] J. Xiao, J. Liu, Z. Lv, X. Shi, and J. Han, "On-axis near-eye display system based on directional scattering holographic waveguide and curved goggle," Opt. Express 27(2), 1683-1692 (2019).

[7] C. Yoo, K. Bang, C. Jang, D. Kim, C. K. Lee, G. Sung, and B. Lee, "Dual-focal waveguide see-through near-eye display with polarization-dependent lenses," Opt. letters 44(8), 1920-1923 (2019).

[8] J. D. Waldern, R. Morad, and M. M. Popovich, "Waveguide Manufacturing for AR Displays, Past, Present and Future," Frontiers in Optics, FW5A-1 (2018).

[9] G. Quaranta, G. Basset, O. J. Martin, and B. Gallinet, "Recent advances in resonant waveguide gratings," Laser & Photonics Reviews 12(9), 1800017 (2018).

[10] Lee, G. Y., Hong, J. Y., Hwang, S., Moon, S., Kang, H., Jeon, S. & Lee, B. (2018). Metasurface eyepiece for augmented reality. Nature communications, 9(1), 4562.

[11] Y. Amitai, "P-21: Extremely Compact High‐Performance HMDs Based on Substrate‐Guided Optical Element," SID Symposium Digest of Technical Papers 35(1), 310-313 (2004).

[12] Y. Amitai, "P-27: A Two‐Dimensional Aperture Expander for Ultra‐Compact, High‐Performance Head‐Worn Displays," SID Symposium Digest of Technical Papers 36(11), 360-363 (2005).

[13] D. Cheng, Y. Wang, C. Xu, W. Song, and G. Jin, "Design of an ultra-thin near-eye display with geometrical waveguide and freeform optics," Opt. Express 22(17), 20705-20719 (2014).

[14] B. Pascal, D. Guilhem, and S. Khaled, "Optical guide and ocular vision optical system," U.S. Patent, No. 8,433,172 (2013).

[15] K. Sarayeddline, K. Mirza, P. Benoit, and X. Hugel, "Monolithic light guide optics enabling new user experience for see-through AR glasses," Photonics Applications for Aviation, Aerospace, Commercial, and Harsh Environments V 9202-92020 (2014).

[16] K. Sarayeddine and K. Mirza, "Key challenges to affordable see-through wearable displays: the missing link for mobile AR mass deployment." Photonic Applications for Aerospace, Commercial, and Harsh Environments IV 8720-87200 (2013).

[17] M. Xu and H. Hua, "Ultrathin optical combiner with microstructure mirrors in augmented reality," SPIE-Proceedings (Digital Optics for Immersive Displays) **10676**, 1067614 (2018).

[18] M. Xu and H. Hua, "Methods of optimizing and evaluating geometrical lightguides with microstructure mirrors for augmented reality displays," Opt. Express **27**(4), 5523-5543 (2019).